Journal of Materials Chemistry A

Accepted Manuscript

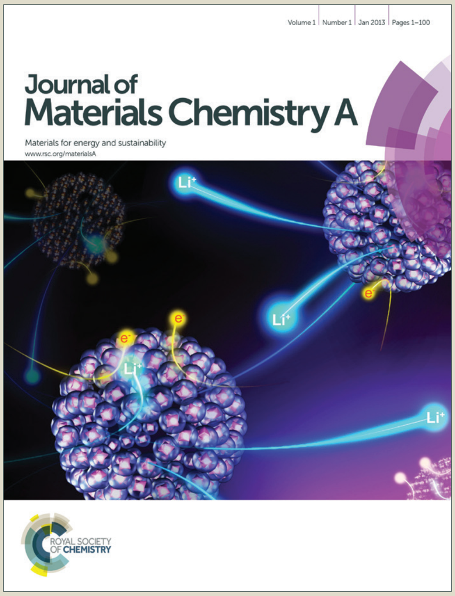

ROYAL SOCIETY OF CHEMISTRY

www.rsc.org/materialsA

Ionothermal confined self-organization for hierarchical porous magnesium borate superstructures as high efficient adsorbents for dye removal

Zhaoqiang Zhang[a], *Wancheng Zhu*[a,*], *Ruguo Wang*[a], *Linlin Zhang*[a], *Lin Zhu*[a], *Qiang Zhang*[b,*]

[a] Department of Chemical Engineering, Qufu Normal University, Shandong 273165, China.

[b] Beijing Key Laboratory of Green Chemical Reaction Engineering and Technology, Department of Chemical Engineering, Tsinghua University, Beijing 100084, China.

---

[*] Corresponding author. Tel.: +86-537-4453130; fax: +86-10-62772051.

E-mail: zhuwancheng@tsinghua.org.cn (W. Zhu); zhang-qiang@mails.tsinghua.edu.cn (Q. Zhang).

Abstract: Three-dimensional (3D) hierarchical porous structures self-organized by one-dimensional (1D) building blocks have attracted much concern due to their unique properties and versatile applications. Herein, uniform hierarchical porous $MgBO_2(OH)$ superstructures with microsphere-like profile were synthesized for the first time *via* a facile ionothermal synthesis (150 ºC,12.0 h), by using $MgCl_2$, H_3BO_3, NaOH as the raw materials and N,N-dimethylformamide nitrate ionic liquid as the solvent. The porous $MgBO_2(OH)$ microspheres exhibited a specific surface area of 57.22 m^2 g^{-1}, 82.4% of which had a diameter within the range of 4.0-6.0 μm. The subsequent mild thermal conversion (600 ºC,12.0 h) gave rise to the hierarchical porous $Mg_2B_2O_5$ microspheres with high crystallinity and a specific surface area of 24.20 m^2 g^{-1}. The synergistic effect of the hydrophilic surfaces of the $MgBO_2(OH)$ nanostructures and the ionothermal confined self-organization co-contributed to the formation of the hierarchical porous $MgBO_2(OH)$ and $Mg_2B_2O_5$ superstructures, which were employed as the adsorbents for the adsorption of Congo red (CR) from the simulated waste water, and both of the $MgBO_2(OH)$ and $Mg_2B_2O_5$ superstructures exhibited good recyclability and reusability as high efficient adsorbents for dye removal after regeneration. The Langmuir isothermal model well interpreted the adsorption behavior of CR and the intra-particle diffusion model was also well fitted based on the kinetic data, indicating the microsphere diffusion as the rate-limiting step, and the maximum adsorption capacities q_m for CR onto the porous $MgBO_2(OH)$ and $Mg_2B_2O_5$ superstructures calculated from the Langmuir isothermal model were 228.3 and 139.3 mg g^{-1}, respectively. The present ionothermal confined self-organization for the hierarchical porous $MgBO_2(OH)$ and $Mg_2B_2O_5$ superstructures provided new insights into the materials chemistry and controllable ionothermal route to hierarchical borate nanoarchitectures, and also waved new platform for dye adsorption, and other potential fields such as heterogeneous catalysis.

Keywords: ionothermal, confined self-organization, hierarchical, porous, magnesium borate, adsorption

1. **Introduction**

Three-dimensional (3D) hierarchical micro-/nanostructured materials, self-assembled or self-organized by one-dimensional (1D) and two-dimensional (2D) building blocks, have attracted extensive attention due to their unique size- and morphology-dependent properties as well as novel applications which make them more and more practical.[1-5] Among the multitudes of 1D nanostructures or 1D nanostructured building blocks constructured hierarchical metal oxides, carbonates, silicates, and so forth, 1D magnesium borate nanostructures (*e.g.* $Mg_2B_2O_5$ nanowires,[6-8] nanorods[9, 10] and whiskers,[11-13] MgB_4O_7 nanowires,[14] $Mg_3B_2O_6$ nanotubes[15]) have been highly considered for their excellent performances when employed as reinforcements in the wide band gap semiconductors,[6] electronic ceramics,[14] antiwear additive,[16] and plastics or aluminum/magnesium matrix alloys.[17] As a matter of fact, in addition to traditional high temperature techniques such as chemical vapor deposition (CVD)[6, 9, 10, 14, 15] and molten salt synthesis (MSS)[18-20] for anhydrous 1D magnesium borate nanoarchitectures, hydrated and anhydrous 1D magnesium borate nanorods/nanowires/nanowhiskers have also been available by hydrothermal synthesis[8, 21-23] or hydrothermal based thermal conversion (HTC).[12, 24, 25]

The templated hydrothermal or solvothermal synthesis has been widely used for hierarchical nanostructures fabrication,[2, 26, 27] although there are technical bottlenecks on the impurity introduction and the inevitable structural collapse during the post-treatment for template removal. Comparatively, the temperature range for the liquid phase of water (0-100 ºC) is relatively narrow, which limits the application of the hydrothermal synthesis for those require lower or higher temperature.[28] In contrast, solvothermal synthesis using organic solvents as media might suffer from the relatively low solubility of the inorganic reactants and also potential security problems for the intrinsic nature of the organic solvents such as toxic, flammable, and even explosive.[29] It is thus highly desirable to seek alternative solvents, which possess tunable and versatile solvent properties, with easy disposal of the templates as well as the facile, green, and reliable synthesis of inorganic materials.

Ionic liquids (ILs), entirely consisted of ions, have attracted considerable attention and upsurge of interests owing to their distinct physical and chemical properties, such as low melting points (below 100 ºC), excellent thermal stability, negligible vapor pressure, and wide temperature range of dissolving ability for both organic and inorganic compounds.[30] ILs have been more and more extensively exploited as competitive alternatives for traditional solvents in multitudes of fields, such as catalysis, separations, and electrochemistry.[28, 31] Nowadays, although many inorganic materials with novel morphologies and unique properties, including novel porous carbon,[1] hematite,[32] lithium iron phosphate,[33] etc., have been available *via* ILs mediated or ionothermal synthesis, there are still much way to go for such booming domain both in controllable synthesis and intrinsic mechanism. To date, there are still few reports on the ionothermal synthesis of borate nanostructures, not to mention the hierarchical borates superstructures. If the aforementioned 1D magnesium borates were self-organized into 3D hierarchical and even porous superstructures, their dispersion in the polymer/metal/ceramic matrix would be expected to be greatly improved, and their applications could be further broadened to other areas such as water treatment, catalysis, as well as energy storage.

Recently, 3D flower-like $Mg_3B_2O_6$ microspheres assembled by nanosheets were synthesized via a poly(vinyl pyrrolidone) (PVP) assisted precipitation reaction and sequential calcination (650 ºC,4.0 h).[34] The mesoporous $2MgO\cdot B_2O_3$ microspheres whereas with very low crystallinity were fabricated *via* a similar precipitation process followed by calcination (500 ºC-4.0 h), using sodium dodecyl sulfates (SDS) as template.[35] To further enlarge the applications of magnesium borates, to date it was however still a tough issue and great challenge to acquire 3D hierarchical magnesium borate superstructures with relatively high crystallinity and porous structure.

In our previous work, 1D $Mg_2B_2O_5$ nanowhiskers[12, 24, 25] have been obtained based on the controllable hydrothermal formation of the $MgBO_2(OH)$ nanowhiskers.[21, 36] Herein, we reported for the first time our latest investigation on the facile ionothermal synthesis of the hierarchical porous $MgBO_2(OH)$ superstructures, followed by the subsequent thermal conversion and which led to hierarchical porous $Mg_2B_2O_5$ superstructures. The possible formation mechanism was discussed. Moreover, the as-obtained hierarchical porous $MgBO_2(OH)$ and $Mg_2B_2O_5$ superstructures were both evaluated as novel recyclable adsorbents for toxic organic chemicals such as Congo Red (CR) from the simulated waste water.

2. Results and discussion

2.1. Ionothermal synthesis of hierarchical $MgBO_2(OH)$ superstructures

The pre-prepared $DMFH^+$ NO_3^- ILs was employed as the medium for the ionothermal synthesis. **Fig. 1** shows the composition, profile, and size distribution of the ionothermal product synthesized at 150 ºC for 12.0 h. As shown (**Fig. 1a**), all the diffraction peaks of the XRD pattern were readily indexed to those of the standard monoclinic $MgBO_2(OH)$ (JCPDS No. 39-1370), and no other peak of impurity was detected. Notably, the pure crystal phase of the present ionothermal product was same with the $MgBO_2(OH)$ nanowhiskers derived from the hydrothermal synthesis, however the strongest diffraction peak was located at $2\theta = 33.76$ º and the corresponding planes were $(\bar{1}21)$. This was different with the generally strongest diffraction peak that corresponded with (200) planes, which were parallel with the longitudinal and also preferential growth direction of the $MgBO_2(OH)$ nanowhiskers.[21, 36] The crystallite size D_{200} here calculated by the Debye-Scherrer equation was 12.3 nm, indicating the approximate size perpendicular to (200) planes, *i.e.* along the latitudinal direction of the 1D $MgBO_2(OH)$ nanostructures.

The typical SEM image demonstrates the ionothermal products of hierarchical porous $MgBO_2(OH)$

superstructures, containing multitudes of constitutional 1D nanobuilding blocks or subunits. The superstructures emerged uniform microsphere-like profile and narrow diameter distribution (**Fig. 1(b)**), and 82.4% of the as-obtained superstructures have a diameter within the range of 4.0-6.0 μm (**Fig. 1(b_1)**). Moreover, some porous microspheres exhibited remarkable inner cavities within the spherical body, denoted as the yellow dotted-circle areas. High-magnification SEM image (**Fig. 1(c)**) clearly revealed that the as-synthesized $MgBO_2(OH)$ superstructures consisted of multitudes of seemingly randomly stacked short tiny 1D nanofloccules or nanorods, whereas with profound spherical profiles and distinct cavities on the peripheral surfaces of the microspheres. The constitutional 1D nanorods had a length less than 1.0 μm, much shorter than the previously hydrothermally obtained nanowhiskers at 240 ºC for 18.0 h.[21, 36] In addition, both the low-magnification (**Fig. 1(d)**) and high-magnification TEM images corresponding to the local surface (**Fig. 1(d_1)**) or the group of 1D subunits segregated from the bulk due to the ultrasonication in the course of sample preparation (**Fig. 1(d_2)**) reconfirmed the as-obtained microspheres of hierarchical porous superstructures. Obviously, such hierarchical porous superstructures with well defined spherical profile were quite different from the agglomerated urchin-like spherical $MgBO_2(OH)$ clusters.[23]

2.2. Thermal conversion for hierarchical $Mg_2B_2O_5$ superstructures

Thermal decomposition property of the $MgBO_2(OH)$ superstructures was evaluated by the simultaneously recorded thermogravimetric-differential scanning calorimetric (TG-DSC) curves, as shown in **Fig. 2**. The sample mass decreased at a slow rate below 295 ºC, a relatively fast rate within 295-440 ºC, a significantly fast rate within 440-595 ºC, a slight slow rate within 650-800 ºC, and kept almost constant thereafter. The gradual mass decrease before 440 ºC was owing to the elimination of the physically absorbed water and the residual of ILs[37] that absorbed onto and inside of porous superstructures. The subsequent mass loss of 10.4% between 440 and 595 ºC was quite similar to the theoretical weight loss (10.7%) for the conversion of $MgBO_2(OH)$ to $Mg_2B_2O_5$.[9] Notably however, there was also a slight slow rate of mass loss from 650 to 800 ºC, which might be ascribed to the partial conversion of $Mg_2B_2O_5$ to $Mg_3(BO_3)_2$ as follows:[12, 25]

$$3Mg_2B_2O_5 \rightarrow 2Mg_3(BO_3)_2 + B_2O_3 \qquad (1)$$

The final decomposition temperature (595 ºC) of $MgBO_2(OH)$ superstructures was lower than that of the $MgBO_2(OH)$ nanowhiskers (620 ºC)[25] whereas much lower than that of natural szaibelyite ($MgBO_2(OH)$, 700 ºC),[38] ascribed to the small size effect. The simultaneously recorded DSC curve exhibited a broad endothermic peak within 440-595 ºC, in accordance with the dehydration of the structural water from $MgBO_2(OH)$ superstructures. The slight endothermic effect between 595-650 ºC should be associated with the partial decomposition of $Mg_2B_2O_5$ for $Mg_3(BO_3)_2$. Distinctly, there emerged a sharp exothermic peak at 650-680 ºC on account of the recrystallization of $Mg_2B_2O_5$,[38] and this was also consistent with our previous work.[25]

Fig. 3 shows the composition, profile and size distribution of the calcined product derived from the thermal conversion of the ionothermally synthesized $MgBO_2(OH)$ superstructures at 600 ºC for 12.0 h with a heating rate of 5 ºC min^{-1}. As shown in **Fig. 3(a),** each diffraction peak of the XRD pattern could be assigned to that of the standard triclinic $Mg_2B_2O_5$ (JCPDS No. 73-2232). The crystallinity of the as-obtained $Mg_2B_2O_5$ superstructures was somehow lower than the triclinic $Mg_2B_2O_5$ nanowhiskers calcined by $MgBO_2(OH)$ nanowhiskers in the absence of NaCl at 650-700 ºC for 2.0 h,[24] whereas much higher than the mesoporous $2MgO{\cdot}B_2O_3$ microspheres.[35] The as-calcined superstructures were of hierarchical porous structures with well preserved profile of $MgBO_2(OH)$ microspheres (**Fig. 3(b)**). There were cavities within the body of the porous microspheres, as denoted by the yellow dashdotted-line circles areas. Meanwhile, the size distribution (**Fig. 3(b$_1$)**) indicated that *ca.* 80% of the $Mg_2B_2O_5$ superstructures had a diameter within the range of 3.0-5.0 μm, somehow smaller than that of the ionothermally synthesized

$MgBO_2(OH)$ superstructures owing to the dehydration. Moreover, the high-magnification SEM image (**Fig. 3(c)**) clearly revealed that the $Mg_2B_2O_5$ superstructures were composed of numerous tiny nanorods with smaller size due to the pore shrinkage in the course of thermal conversion, compared with the constitutional nanorods within the $MgBO_2(OH)$ superstructures. The TEM images (**Fig. 3(d, d_1)**) reconfirmed the as-calcined hierarchical porous superstructures of well defined spherical profile and constitutional tiny nanorods.

To better understand the thermal decomposition properties of the ionothermally synthesized $MgBO_2(OH)$ superstructures, the calcination temperature, time, and also heating rate were tuned within the range of 600-700 ºC, 2.0-8.0 h, and 2-10 ºC min^{-1}, respectively, so as to investigate the corresponding effect on the calcined products. As shown in **Fig. S1,** the pure phase of triclinic $Mg_2B_2O_5$ (JCPDS No. 73-2232) was available when calcined at 600 ºC for various growth durations and at various heating rates. However, when calcined at higher temperature such as 700 ºC, a mixture of triclinic $Mg_2B_2O_5$ and $Mg_3(BO_3)_2$ (JCPDS No. 33-0858) were obtained.

2.3. Hierarchical porous structures within the $MgBO_2(OH)$ and $Mg_2B_2O_5$ microspheres

The typical nitrogen adsorption-desorption isotherms were recorded to determine the porous structures within the $MgBO_2(OH)$ and $Mg_2B_2O_5$ microspheres, as shown in **Fig. 4**. Both the sorption isotherms of $MgBO_2(OH)$ (**Fig. 4(a)**) and $Mg_2B_2O_5$ (**Fig. 4(b)**) superstructures demonstrated as type IV with H3-type hysteresis loops according to Brunauer-Deming-Deming-Teller classification, revealing the dominant narrow slit-shaped mesopores within the superstructures.[39] Comparatively, however, the sorption isotherms of the $Mg_2B_2O_5$ microspheres displayed a narrower hysteresis loop at relatively high pressure as P/P_0=0.8-1.0, indicating the constitutional macropores within the calcined loose superstructures. Meanwhile, the pore size distribution (PSD) indicated that the $MgBO_2(OH)$ superstructures contained a few mesopores and abundant macropores. Moreover, the $Mg_2B_2O_5$ microspheres contained more textural mesopores with pore diameter within the range of 3-5 nm, owing to the dehydration in the thermal conversion process. Taking the size of the constitutional tiny nanorods within the superstructures into consideration, the mesopores should be due to the N_2 sorption measurement ($MgBO_2(OH)$) or previous dehydration ($Mg_2B_2O_5$), whereas the macropores should be mainly derived from the organization of the nanorods building blocks within the superstructures. Notably, the $Mg_2B_2O_5$ microspheres contained more macropores than the $MgBO_2(OH)$ microspheres due to the thermal conversion, in accordance with the SEM observation (**Fig. 1(c), Fig. 2(c)**).

The hierarchical porous $MgBO_2(OH)$ microspheres exhibited a specific surface area of 57.22 $m^2\ g^{-1}$, a pore volume of 0.32 $cm^3\ g^{-1}$, and an average pore radius of 1.85 nm. The specific surface area was somewhat larger than that of the mesoporous $2MgO{\cdot}B_2O_3$ microspheres (53.03 $m^2\ g^{-1}$),[35] after the thermal conversion, the as-obtained hierarchical porous $Mg_2B_2O_5$ microspheres demonstrated a specific surface area of 24.20 $m^2\ g^{-1}$, a pore volume of 0.20 $cm^3\ g^{-1}$ and an average pore radius of 2.06 nm. Apparently, the specific surface area was slightly decreased when compared with that of the porous $MgBO_2(OH)$ microspheres precursor. Nevertheless, the hierarchical porous $MgBO_2(OH)$ and $Mg_2B_2O_5$ microspheres with high crystallinity revealed them of great potential applications for adsorption, and so forth.

2.4. Formation mechanism of hierarchical porous $MgBO_2(OH)$ and $Mg_2B_2O_5$ superstructures

No doubt, the ionothermal treatment has played the key role in the formation of the $MgBO_2(OH)$ and $Mg_2B_2O_5$ superstructures. As a matter of fact, the resultant white slurry containing NaOH, $MgCl_2{\cdot}6H_2O$ and H_3BO_3 could not completely dissolve into the ILs whereas could be thoroughly water soluble. Taking the phase change before and after the ionothermal treatment into consideration, the corresponding ionic reactions could be written as follows:

$$MgCl_2\cdot 6H_2O\,(aq.) \rightarrow Mg^{2+}\,(aq.) + 2Cl^-\,(aq.) + 6H_2O \qquad (2)$$

$$H_3BO_3\,(s) + H_2O \rightarrow B(OH)_4^-\,(aq.) + H^+\,(aq.) \qquad (3)$$

$$NaOH\,(aq.) \rightarrow Na^+\,(aq.) + OH^-\,(aq.) \qquad (4)$$

$$B(OH)_4^-\,(aq.) + Mg^{2+}\,(aq.) + OH^-\,(aq.) \rightarrow MgBO_2(OH)\,(s) + 2H_2O \qquad (5)$$

The overall ionothermal chemical conversion could thus be expressed as follows:

$$MgCl_2\,(aq.) + H_3BO_3\,(s) + 2NaOH\,(aq.) \rightarrow MgBO_2(OH)\,(s) + 2NaCl\,(aq.) + 2H_2O \qquad (6)$$

This was different from the previous hydrothermal formation of the $MgBO_2(OH)$ nanowhiskers, which was derived from the hydrothermal conversion of the amorphous intermediate, *i.e.* the room temperature coprecipitate $Mg_7B_4O_{13}\cdot 7H_2O$.[36] Notably however, in addition to the water derived from the reactant $MgCl_2\cdot 6H_2O$ (eqn. (2)), there was also some amount of water formed according to eqn. (5), even under the deliberately designed ionothermal conditions.

To better understand the intrinsic mechanism, the effects of ionothermal temperature and time on the product were investigated, as shown in **Fig. S2** and **S3**, respectively. When ionothermally treated at 70 ºC, no solid state product was available. When ionothermally treated at various temperatures above 100 ºC for 12.0 h (**Fig. S2**), the products were all confirmed as pure phase of $MgBO_2(OH)$ (JCPDS No. 39-1370), and the crystallinity of the product became higher with the increase in the temperature within 100-180 ºC. After ionothermally treated at 120 ºC, the product exhibited poor crystallinity and short nanorod-like morphology (**Fig. S2(a$_1$,b)**), which was ascribed to the initial anisotropic growth of $MgBO_2(OH)$ in the ILs and was somehow similar to the hydrothermal formation of the $MgBO_2(OH)$ at 100-120 ºC with rudimental 1D morphology.[40] With the temperature increasing to 140 ºC, the product became quasi-spherical $MgBO_2(OH)$ assemblies with non-uniform PSD (**Fig. S2(a$_2$,c)**). When the temperature went up to 150 and 160 and further 180 ºC, the product was confirmed as uniform hierarchical porous microspheres (**Fig. 1**), which however evolved into porous microspheres with relatively broad PSD (**Fig. S2(a_3,d)**) and further turned out to be quasi-spherical disassemblies owing to over high temperature ionothermal treatment (**Fig. S2(a_4,e)**).

When ionothermally treated at 150 ºC for various time, similar growth phenomena were observed. The crystallinity got higher with the extending of the time from 6.0 to 16.0 h. As for the 6.0 h of ionothermal treatment, the low crystallinity and rudimental spherical $MgBO_2(OH)$ assemblies (**Fig. S3(a_1,b)**) were available. With the time extending to 8.0 (**Fig. S3(a_2,c)**) and 10.0 (**Fig. S3(a_3,d)**) and 12.0 h (**Fig. 3**), the products became increasingly uniform with distinct spherical profile and hierarchical porous structures (denoted as the red dotted-circle region in **Fig. S3(d**) and yellow dashdotted-line circles region in **Fig. 1(b)**). Nevertheless, when ionothermally treated for over long time such as 16.0 h, the hierarchical porous microspheres became disassembled, resulting in remarkable spindle or bundle-like $MgBO_2(OH)$ architectures containing higher aspect ratio 1D nanostructures (**Fig. S3(a_4,e)**), which was originated from the side-by-side oriented growth of the $MgBO_2(OH)$ nanowhiskers along the (200) planes.[40] The disassembly growth phenomena of the hierarchical porous $MgBO_2(OH)$ superstructures here in case of over ionothermal treatment, *e.g.* at higher temperature than 150 ºC for longer time than 12.0 h, was somehow similar to that ascertained in the hydrothermal formation of the laminar rhombic $Ca_4B_{10}O_{19}\cdot 7H_2O$ superstructures.[41]

Based on the above experimental results, a formation mechanism of the hierarchical porous $MgBO_2(OH)$ as well as $Mg_2B_2O_5$ superstructures was proposed, as illustrated in **Fig. 5**. Firstly, water derived from the reactant led to spherical water bubbles or reservoirs due to the surface tension for reducing the overall energy within the ILs, which favored and trapped the continuously dissolved Mg^{2+}, $B(OH)_4^-$ and OH^- ions from the deposited solid reactants, resulting in the milk-white and quasi-w/o microemulsion system under constant magnetic stirring; Secondly, with the ionothermal temperature increasing, the trapped Mg^{2+},

$B(OH)_4^-$ and OH^- ions within the reservoirs reacted with each other, producing original $MgBO_2(OH)$ nanostructures with rudimental 1D nanorod-like morphology at the cost of continuously dissolution of the reactants; Thirdly, with the ionothermal treatment going on, the newly dissolved ions migrated into the reservoirs continuously, not only serving as the requisite nutrients for the heterogeneous or homogeneous nucleation but also somehow pushing the pre-formed nanorods to move outwards to the interfaces between the water and ILs; Fourthly, the hydrophilic effect of the nanorods' surfaces rendered the stable ionothermal confined self-organization of the $MgBO_2(OH)$ nanorods and thus brought about the uniform hierarchical porous $MgBO_2(OH)$ superstructures with microsphere-like profile; Finally, subsequent mild thermal conversion gave rise to the final formation of the hierarchical porous $Mg_2B_2O_5$ superstructures with the precursors' microsphere-like profile well preserved.

2.5. Synergistic effect of hydrophilic surfaces and ionothermal confined self-organization

Apparently, the hydrophilic effect based and ionothermal confined self-organization was responsible for the formation of the present $MgBO_2(OH)$ and $Mg_2B_2O_5$ hierarchical porous superstructures. Nevertheless, the 1D $MgBO_2(OH)$ nanorods could not fully grow due to the confinement of the water bubbles within the ILs, compared with those grown at the same temperature for time under hydrothermal conditions. As confirmed in **Fig. S4**, with the volume ratios of ILs/water decreasing from 8/1 to 3/1 to 2/1 and to 0/1, the aspect ratio of the 1D $MgBO_2(OH)$ nanostructures became higher and higher. Simultaneously however, with the increases in the amount of water, the self-organization of the 1D building blocks became increasingly blurred and even disappeared. Consequently, an optimal amount of water bubbles were crucial for the ionothermal confined self-organization for the present hierarchical porous $MgBO_2(OH)$ superstructures. More water was favorable for the growth of high aspect ratio $MgBO_2(OH)$ nanostructures rather than the corresponding ionothermal confined self-organization. In other words, the $MgBO_2(OH)$ nanostructures exhibited hydrophilic surfaces, which favored their preferential growth into high aspect ratio nanostructures in an hydrous environment.

Until now, the roles of the ILs during the synthesis of inorganic materials were viewed as solvent,[42] template,[43] direction agents,[44] capping agents, stabilizing agents,[33] or modifying agents.[45] To obtain new insight into the specific role of the present ILs in the ionothermal self-organization of the hierarchical porous $MgBO_2(OH)$ microspheres, a series of control experiments were undertaken using DMF, DMA, the miscible liquids of HNO_3 and DMF, as well as the liquid recovered from the former ionothermal treatment as solvents (**Fig. S5**). All the products (**Fig. S5(a-d)**) were confirmed as $MgBO_2(OH)$ phase (XRD patterns not shown here), however only the recovered liquid from the former ionothermal synthesis promoted the formation of the $MgBO_2(OH)$ microspheres (**Fig. S5(d)**), indicating the present ILs requisite in the ionothermal self-organization of the hierarchical porous superstructures on the one hand and relatively good recyclability of the ILs on the other hand. As a matter of fact, when using the liquid that collected from the previously heat treated DMF (150 ºC,12.0 h) as solvent, no solid state product was available at all. This revealed the decomposition product of DMF (150 ºC,12.0 h) could not favor the formation of the $MgBO_2(OH)$ phase, not to mention the corresponding self-organization. Therefore, ILs probably served as a liquid solvent that could form a stable quasi-w/o microemulsion system when containing applicable amount of water bubbles, which would further create the confinement effect during the ionothermal formation of the $MgBO_2(OH)$ microspheres. This was very similar to the effect of ILs in the synthesis of Bi_2S_3 nanostructures reported by Jiang *et al.*[46] Thus, it should be the synergistic effect of the hydrophilic surfaces of the $MgBO_2(OH)$ nanostructures and the ionothermal confined self-organization that co-contributed to the formation of the hierarchical porous $MgBO_2(OH)$ superstructures. However, the over ionothermal treatment, *i.e.* ionothermally treated at excessively high temperature (higher than 160 ºC) for excessively long time (longer than 16.0 h), induced lower stability of the ILs. This in turn affected the formation of the quasi-w/o microemulsion system and thus restrained the further ionothermal confined self-organization for the hierarchical porous superstructures.

2.6. Dye adsorption on hierarchical porous $MgBO_2(OH)$ and $Mg_2B_2O_5$ superstructures

The as-synthesized hierarchical porous $MgBO_2(OH)$ and $Mg_2B_2O_5$ superstructures were employed as the adsorbents for CR removal from the simulated waste water, which was known as a secondary diazo dye of the representative organic pollutant commonly used in the cotton textile, wood pulp, and paper industries, with a characteristic UV-vis adsorption at *ca.* 496 nm. As shown in **Fig. 6a**, both porous superstructures exhibited satisfactory adsorption rates, since the C_t/C_0 value for the adsorption of CR onto $MgBO_2(OH)$ and $Mg_2B_2O_5$ superstructures reached relatively constant within 40 and 140 min, respectively. The removal efficiency of the CR from the simulated solution rapidly approached to *ca.* 94.21% and 90.89% within 120 min for $MgBO_2(OH)$ and $Mg_2B_2O_5$ porous microspheres, respectively, and both turned to slow and steady thereafter. The adsorption rate of the $MgBO_2(OH)$ porous microspheres was faster than that of the $Mg_2B_2O_5$ porous microspheres, and the variation of the adsorption capacity with the contact time was shown in **Fig. 6b**. Apparently, the adsorption capacity of the $MgBO_2(OH)$ porous microspheres at any time, *i.e.* q_t, was also higher than that of the $Mg_2B_2O_5$ porous microspheres almost within the whole adsorption time range. The faster adsorption rate as well as higher adsorption capacity for CR onto the $MgBO_2(OH)$ porous microspheres should be attributed to the correspondingly larger specific surface area, pore volume, as well as the specific surface properties of the porous superstructures.

The analysis of the adsorption isotherm was essential to understand the adsorption mechanism of the adsorbate molecules distribution among liquid and adsorbent, according to a series of assumptions those related to the heterogeneity/homogeneity of adsorbents, the type of coverage, and the possibility of interaction between the adsorbate molecules.[47] As known, the Langmuir isotherm model and Freundlich isotherm model are typical mathematical models those have been widely employed for the investigation on the adsorption mechanisms. The former model was based on the assumption that all sorption sites on the adsorbent are identical and energetically equivalent, and the latter one was on account of that the adsorption is a multilayer adsorption on heterogeneous surfaces, reversible and in heterogeneous systems. In a word, Langmuir isotherm indicates monolayer coverage, whereas Freundlich isotherm reveals no restriction. Mathematically, the Langmuir model and Freundlich model can be expressed as eq. (7) and (8), respectively:

$$q_e = \frac{q_m b c_e}{1 + b c_e} \tag{7}$$

$$q_e = k_f c_e^{1/n} \tag{8}$$

where q_e is the amount of adsorbed CR on the adsorption surfaces at equilibrium (mg g^{-1}), q_m is the theoretical maximum adsorption capacity (mg g^{-1}), b is the coefficient related to the energy of adsorption, c_e is the concentration of the CR in solution at equilibrium (mg L^{-1}). As for the Freundlich model, k_f and $1/n$ are constants correlated to the adsorption capacity at the unit concentration and the adsorption intensity, respectively.

The experimental data for the adsorption of CR was fitted with both of the above two models, as presented in **Fig. 7**. When fitted with the Langmuir model, the correlation coefficients R^2 of the hierarchical porous $MgBO_2(OH)$ and $Mg_2B_2O_5$ superstructures were both 0.9903 (**Table S1**), much higher than those of the hierarchical porous $MgBO_2(OH)$ and $Mg_2B_2O_5$ superstructures fitted with Freundlich model (0.8890 and 0.8766), respectively (**Table S1**). Thus, compared with the Freundlich model, the Langmuir model presented a quite satisfactory fitting result, which revealed that the adsorption of CR on the as-obtained hierarchical porous $MgBO_2(OH)$ and $Mg_2B_2O_5$ superstructures was of a monolayer adsorption process. In other words, the sites that had been occupied by adsorbate molecules could not further undergo adsorption and there was no strong interaction among adsorbate molecules. The maximum adsorption capacities of CR adsorption onto the hierarchical porous $MgBO_2(OH)$ and $Mg_2B_2O_5$ superstructures derived from the Langmuir isotherm model were 228.3 and 139.3 mg g^{-1}, respectively (**Table S1**).

The present prominent removal efficiency of CR was believed to be associated with the specific hierarchical porous structures within the microspheres, and the maximum adsorption capacity for CR via various adsorbents were also compared, as listed in the **Table 1**. Both of the $MgBO_2(OH)$ and $Mg_2B_2O_5$ porous microspheres exhibited relatively higher adsorption abilities than some traditional oxides such as Fe_3O_4 microspheres,[48] urchin-like α-Fe_2O_3,[49] α-Fe_2O_3 hollow structures,[50] and so on. However, the q_m did not get higher monotonously with the increase in the specific surface area of the adsorbents, indicating probable additional electrostatic interaction between CR and the adsorbents which also played a significant role in determining the adsorption efficiency. Meanwhile, the q_m of the $MgBO_2(OH)$ microspheres was much higher than that of the $Mg_2B_2O_5$ microspheres, probably ascribed to the larger surface area and the interactions between –OH and CR molecules. Moreover, the q_m of the $MgBO_2(OH)$ microspheres was even larger than that of hollow nestlike α-Fe_2O_3 spheres[51] and hierarchical spindle-like γ-Al_2O_3[52] with impressively larger specific surface areas, reconfirming the paramount important factor determining the adsorption capacity was not really the specific surface area. Notably however, the q_m of the $MgBO_2(OH)$ microspheres was smaller than that of the MgO (111) nanoplates[53] and CdO cauliflower-like nanostructures,[54] because of the relatively smaller specific surface area of the former on the one hand, and also a strong electrostatic interaction between the latter adsorbents with the employed dye species on the other hand. On the whole nevertheless, the adsorption test confirmed the as-obtained porous $Mg_2B_2O_5$ especially $MgBO_2(OH)$ microspheres as an ideal adsorbent candidate for CR containing water treatment. In addition to the specific surface area nature of the porous structures, the electrostatic interaction between the present hierarchical porous microspheres and the employed CR dye should be more responsible for the satisfactory adsorption performance, which however still needed further investigation so as to get deeper understanding.

To further evaluate the adsorption mechanism of CR onto the hierarchical $MgBO_2(OH)$ and $Mg_2B_2O_5$ superstructures, three typical kinetic models were adopted to interpret the adsorption data, in which however, the pseudo-first-order and pseudo-second-order kinetic models were mostly used. The pseudo-first-order kinetic model (*i.e.* Lagergren's kinetic model) is commonly employed for the adsorption in aqueous solution, depicted as follows:

$$\log\ (q_e - q_t) = \log\ q_e - \frac{k_1}{2.303}t \qquad (9)$$

where q_e and q_t (mg L^{-1}) were the amounts of CR adsorbed at equilibrium and at time t (min), respectively, k_1 was the rate constant (min^{-1}) and t (min) is the contact time between the adsorbent and adsorbate.

In contrast, the pseudo-second-order kinetic model could be expressed as follows:

$$\frac{t}{q_t} = \frac{1}{k_2 q_e^2} + \frac{t}{q_e} \qquad (10)$$

where k_2 was the pseudo-second-order rate constant (g mg^{-1} min^{-1}), q_e was the amount of CR adsorbed at equilibrium (mg g^{-1}), q_t was the amount of CR adsorbed at any time (mg g^{-1}), and t was the time (min).

When the pseudo-first-order kinetic model was employed, the values of adsorption constant k_1 were calculated from the plot of $\log(q_e\text{-}q_t)$ *vs* t (**Fig. 8a**) for $MgBO_2(OH)$ and $Mg_2B_2O_5$, as listed in the **Table S2.** The fitted correlation coefficients R^2 for the adsorption of CR onto the $MgBO_2(OH)$ and $Mg_2B_2O_5$ microspheres were of 0.6192 and 0.9244, respectively. Meanwhile, both $q_{e,calc1}$ values for the $MgBO_2(OH)$ and $Mg_2B_2O_5$ microspheres calculated using the pseudo-first-order kinetic model were of 26.57 and 57.59 g mg^{-1}, respectively, exhibiting a significant variation with the corresponding experimental values $q_{e,exp}$. Both of the correlation coefficients R^2 and the remarkable gap between the calculated $q_{e,calc1}$ values and the corresponding experimental $q_{e,exp}$ values suggested that, the fitted results by the pseudo-first-order kinetic model were far from satisfactory. Thus, the pseudo-first-order kinetic model could not well shed light on the adsorption kinetics. In other words, the physical adsorption that based on the adsorption force through van der Waals force, π-π force, and hydrogen bond between adsorbent and adsorbate was not the rate-limiting step.

Comparatively, when the pseudo-second-order kinetic model was employed, the linear plot of t/q_t against t was obtained (**Fig. 8**)**,** and the q_e, and k_2 values were also available (**Table S2**). Both of the correlation coefficients R^2 were higher than 0.99, which indicated the adsorption process of CR onto the hierarchical $MgBO_2(OH)$ or $Mg_2B_2O_5$ superstructures was more appropriately interpreted by using the pseudo-second-order kinetic model rather than the pseudo-first-order kinetic model. The $q_{e,calc2}$ for the adsorption of CR onto the hierarchical $MgBO_2(OH)$ or $Mg_2B_2O_5$ superstructures calculated from the pseudo-second-order kinetic model were of 99.01 and 97.09 g mg^{-1}, quite similar to the corresponding experimental values for the concentration of adsorbate $q_{e,exp}$ obtained at equilibrium. Clearly, the $q_{e,calc2}$ values derived from the pseudo-second-order kinetic model were much closer to the corresponding $q_{e,exp}$ values than the $q_{e,calc1}$ values those originated from the pseudo-first-order kinetic model. This revealed that the rate-limiting step for the CR adsorption onto the hierarchical $MgBO_2(OH)$ and $Mg_2B_2O_5$ superstructures should be the chemical adsorption, which was connected with the valence forces through sharing or exchanging electrons between the adsorbent and the adsorbate. This however needed further investigation of the adsorption thermodynamics.

In order to better understand the adsorption mechanism, the intra-particle diffusion model was further investigated so as to verify the possible transportation of CR molecules into the pores of the $MgBO_2(OH)$

and $Mg_2B_2O_5$ microspheres. The model was described as follows:

$$q_t = k_{dif}\sqrt{t} + c \tag{11}$$

where k_{dif} was the intra-particle diffusion rate constant (mg g^{-1} $h^{-1/2}$), and c was the intercept (mg g^{-1}), which implied the thickness of the boundary layer. The larger the intercept c, the greater the contribution of the surface adsorption in the rate controlling step was. If the intra-particle diffusion was rate-limited, the plot of the adsorbate uptake q_t *vs* the square root of time t ($h^{1/2}$) would lead to a linear relationship. As shown in **Fig. 9**, the experimental data were divided into two steps which were fitted with the intra-particle diffusion model, due to the difference in the rate of mass transfer at the initial and final stages of adsorption. Such deviation of the straight lines fitted *via* the origin software indicated that the pore diffusion was not the sole rate-controlling step,[59] similar to the results of CR diffusion into the pores of Eucalyptus wood saw dust.[55]

The first stage in diffusion model was the mass transfer of adsorbate molecules from the bulk solution to the adsorbent surface, or to put it simply, the instantaneous stage was attributed to the macropores diffusion. In contrast, the second linear portion was the intra-particle diffusion to the mesoporous within the $MgBO_2(OH)$ and $Mg_2B_2O_5$ superstructures. To determine the rate-controlling step within the intra-particle diffusion, an attempt was made to confirm the rate constants k_{dif} from the intra-particle diffusion plots (**Fig. 9**), as listed in **Table S3**. By comparing the values of k_{dif} for two stages, the high k_{dif1} and low k_{dif2} values were obtained from the macropores and mesopores diffusion stages, respectively. This revealed that the rate-limiting step was the diffusion in mesopores. As obtained from the intercepts (c_1, c_2) of the fitted lines, the boundary effects played a more significant role in the whole diffusion process than the macropores diffusion did.

2.7. Recyclability and reusability of $MgBO_2(OH)$ and $Mg_2B_2O_5$ superstructures as adsorbents

As known, the recyclability and reusability of the adsorbents were quite important for their practical application. After the adsorption, the original white porous $MgBO_2(OH)$ and $Mg_2B_2O_5$ superstructures became red owing to the adsorption of CR. By calcination for regeneration of the adsorbents, the red $MgBO_2(OH)$ and $Mg_2B_2O_5$ superstructures containing CR turned back to white. The regenerated superstructures were employed for the second and also third time adsorption. As shown in **Fig. S6(a, b)**, after calcination (400 ºC, 2.0 h) for elimination of adsorbed CR, the profile as well as the porous structure of the $MgBO_2(OH)$ and $Mg_2B_2O_5$ microspheres were largely retained. The good preservation of the porous superstructures greatly contributed to their comparable adsorption rate performance (**Fig. S6(c,d)**), when calcined and regenerated for the second and third time. It's apparent that, the adsorption performance of the regenerated adsorbents did not significant decreased during the subsequent second and third time adsorption. When employed in the third circle, the removal efficiency of CR by $MgBO_2(OH)$ porous superstructures within 120 min was confirmed as 91.0%, merely decreased 3.2% compared with newly prepared $MgBO_2(OH)$ superstructures. Simultaneously, the removal efficiency of CR by the second time regenerated $Mg_2B_2O_5$ could reach 86.5%. This profoundly indicated the as-obtained hierarchical porous $MgBO_2(OH)$ and $Mg_2B_2O_5$ superstructures of high efficient adsorbents for dye removal with good recyclability and reusability.

3. Conclusions

Uniform hierarchical porous $MgBO_2(OH)$ superstructures with microsphere-like profile were synthesized *via* a facile ionothermal synthesis (150 ºC,12.0 h), using $MgCl_2$, H_3BO_3, NaOH as the raw materials and N,N-dimethylformamide nitrate ionic liquid as the solvent. The as-synthesized hierarchical porous $MgBO_2(OH)$ superstructures exhibited a specific surface area of 57.22 m^2 g^{-1}, 82.4% of which had a diameter within the range of 4.0-6.0 μm. The mild thermal conversion of the $MgBO_2(OH)$ superstructures

(600 ºC, 12.0 h) gave rise to the hierarchical porous $Mg_2B_2O_5$ superstructures with high crystallinity and a specific surface area of 24.20 m^2 g^{-1}. The synergistic effect of the hydrophilic surfaces of the $MgBO_2(OH)$ nanostructures and the ionothermal confined self-organization co-contributed to the formation of the hierarchical porous $MgBO_2(OH)$ and $Mg_2B_2O_5$ superstructures, which were utilized as the adsorbents for the adsorption of Congo red (CR) from the simulated waste water. The results showed that the hierarchical porous $MgBO_2(OH)$ superstructures exhibited outstanding adsorption capacity compared with other adsorbents in literatures, and also higher than the present $Mg_2B_2O_5$ superstructures. The maximum adsorption capacities q_m for CR onto the porous $MgBO_2(OH)$ and $Mg_2B_2O_5$ superstructures were 228.3 and 139.3 mg g^{-1}, respectively. The isothermal modeling revealed that the Langmuir isothermal model better interpreted the adsorption behavior of CR onto the $MgBO_2(OH)$ and $Mg_2B_2O_5$ superstructures, and the intra-particle diffusion model was also well fitted according to the kinetic data. This suggested the diffusion within the mesopores as the rate-limiting step. The calcination and regeneration of the adsorbents containing CR and reuse for adsorption confirmed the as-obtained $MgBO_2(OH)$ and $Mg_2B_2O_5$ superstructures as high efficient adsorbents for dye removal with good recyclability and reusability. The present ionothermal confined self-organization for hierarchical porous $MgBO_2(OH)$ and $Mg_2B_2O_5$ superstructures provided new insights into the materials chemistry and controllable ionothermal route to hierarchical porous metal borates nanoarchitectures, and also waved new platform for dye adsorption, and other potential fields such as heterogeneous catalysis.

4. Experimental section

4.1. Synthesis of N,N-dimethylformamide (DMF) nitrate ionic liquid

All of the reagents were of analytical grade and used as received without further purification. The N,N-dimethylformamide nitrate ionic liquid ($DMFH^+$ NO_3^-) was obtained by neutralization of DMF with a dilute HNO_3 solution (2.0 M) in a low temperature water bath (*ca.* 5 ºC), and the dilute acid was dropwise added with a volume ratio of DMF:HNO_3 = 1.1:1.0, similar to that reported elsewhere.[37] The resultant colorless liquid was transferred into a rotary evaporator for removal of water, DMF, and HNO_3 residues, and the as-obtained light yellow liquid was collected and purified by vacuum drying at 60 ºC for 12.0 h, giving rise to the final light yellow ILs.

4.2. Ionothermal synthesis of hierarchical porous $MgBO_2(OH)$ superstructures

In a typical procedure, certain amount of NaOH powder was dissolved in 30.0 mL of the as-synthesized ILs until the pH was adjusted to *ca.* 7.0 under constant magnetic stirring at room temperature, resulting in a white emulsion. Then 4.066 g (0.02 mol) $MgCl_2 \cdot 6H_2O$ and 1.855 g (0.03 mol) H_3BO_3 were added to the emulsion successively, which could not completely dissolve into the ILs. After kept stirring for another 10.0 min, the resultant slurry was transferred into a Teflon-lined stainless steel autoclave. The autoclave was sealed, heated to 150.0 ºC and kept in an isothermal state for 12.0 h, with a heating rate of 5.0 ºC min^{-1}. After the above ionothermal conversion, the autoclave was cooled down to room temperature naturally. The as-obtained precipitate was filtered, washed with deionized (DI) water, rinsed with anhydrous absolute ethanol for three times, and finally dried at 60.0 ºC for 24.0 h for characterization. To investigate the influence of temperature and time on the ionothermal formation of the products, the temperature and time were tuned within the range of 120-180 ºC and 6.0-16.0 h, respectively. While to investigate the impact of DI water on the ionothermal process, the volume ratio of ILs to DI water was altered from 8:1 to 3:1, 2:1, and to 0:1, respectively. In addition, to ascertain the role of ILs on the formation of the products, the same reactant system was also conducted using the alternative solvent such as DMF, dimethylamine (DMA), DMF/HNO_3, or liquid collected after the above normal ionothermal reaction (150 ºC,12.0 h) as medium, with other conditions kept the same.

4.3. Thermal conversion for hierarchical porous $Mg_2B_2O_5$ superstructures

The former as-synthesized hierarchical $MgBO_2(OH)$ superstructures were transferred into a porcelain boat located in a horizontal tube furnace, which was heated to 600-700 ºC with a heating rate of 5 ºC min^{-1} and kept under an isothermal condition for 2.0-12.0 h, leading to the hierarchical porous $Mg_2B_2O_5$ superstructures. After calcinations, the product was cooled down to room temperature naturally for further characterization. To investigate the effect of calcination parameters, the temperature, heating rate and time were tuned within 600-700 ºC, 2-10 ºC min^{-1}, 2.0-12.0 h, respectively, whereas with other conditions unchanged.

4.4. Hierarchical porous superstructures as adsorbents for dye removal

Hierarchical porous $MgBO_2(OH)$ and $Mg_2B_2O_5$ superstructures were employed as adsorbents for the removal of Congo Red (CR) from the simulated waste water. Specifically, $MgBO_2(OH)$ (20.0 mg) and $Mg_2B_2O_5$ (20.0 mg) were added to the individually pre-prepared CR containing solutions (40.0 mL), respectively, under vigorous magnetic stirring at room temperature, keeping the initial concentration and adsorption time within the range of 10.0-500.0 mg L^{-1} and 10-300 min, respectively. The adsorption rate of CR by $MgBO_2(OH)$ and $Mg_2B_2O_5$ superstructures was evaluated by the ratio of C_t/C_0, where C_0 and C_t represented the concentration of CR (mg L^{-1}) before and sampled at certain intervals during the adsorption, respectively. Meanwhile, to study the kinetics of adsorption, the adsorption in the CR solution with an initial concentration of 50.0 mg L^{-1} was monitored. The adsorption capacity of the adsorbents for CR was calculated according to the following equation:

$$q_t = \frac{(c_0 - c_t)V}{m} \tag{12}$$

$$q_e = \frac{(c_0 - c_e)V}{m} \tag{13}$$

where q_t was the adsorption capacity at time t (mg g^{-1}), and q_e was the equilibrium adsorption capacity (*i.e.*

the adsorbed mass of CR onto the adsorbents $MgBO_2(OH)$ or $Mg_2B_2O_5$ superstructures under the equilibrium conditions, mg g^{-1}), V was the volume of the employed CR solution (L), c_0 and c_e represented the initial and equilibrium concentrations of the CR solution (mg g^{-1}), respectively, c_t indicated the concentration of the CR solution at any t time, and m was the mass of the introduced adsorbents $MgBO_2(OH)$ or $Mg_2B_2O_5$ (g).

4.5. Evaluation of the recyclability and reusability of $MgBO_2(OH)$ and $Mg_2B_2O_5$ superstructures

After the adsorption, the red $MgBO_2(OH)$ and $Mg_2B_2O_5$ superstructures containing adsorbed CR were collected by centrifugation and regenerated by calcination at 400 ºC for 2.0 h with a heating rate of 2 ºC min^{-1} under air atmosphere, for the decomposition and elimination of CR whereas with the profile and porous structure of $MgBO_2(OH)$ and $Mg_2B_2O_5$ largely preserved. The regenerated adsorbents were employed for the second and third time adsorption so as to evaluate the recyclability and reusability of the porous $MgBO_2(OH)$ and $Mg_2B_2O_5$ superstructures.

4.6. Characterization

The crystal structure of the samples were identified by an X-ray powder diffractometer (XRD, MiniFlex600, Rigaku, Japan) with a Cu K_α radiation (λ = 1.5406 Å) and a fixed power source (40.0 kV, 15.0 mA). The morphology and microstructure of the samples were examined using a field emission scanning electron microscopy (SEM, JSM 7401F, JEOL, Japan, at 3.0 kV) and a high resolution transmission electron microscopy (TEM, JEM-2010, JEOL, Japan, at 120.0 kV). The size distribution of the as-synthesized superstructures was estimated by direct measuring about 100 particles from the typical SEM images. The thermal decomposition behavior was detected by the thermal-gravimetric analyzer (TGA, Netzsch STA 409C, Germany) from 30 to 950 ºC, carried out in dynamic air with a heating rate of 10.0 ºC min^{-1}. The porous structure of the samples was characterized by the N_2 adsorption-desorption isotherms, which were measured at 77 K using a chemisorption-physisorption analyzer (Autosorb-1-C, Quantachrome, Boynton Beach, FL, USA) after the samples had been degassed at 300 ºC for 1.0 h, and the pore sizes were evaluated from the N_2 desorption isothermal using the Barrett-Joyner-Halenda (BJH) method. For adsorption properties evaluation, after the adsorption had been performed for the designated time the filtrate was available using filtration, the as-collected filtrate was further quantitatively analyzed and the absorbency was determined by a UV-vis spectrophotometer (UV-756 CRT, Shanghai Yoke Instrument and Meter Co., LTD, China).

Acknowledgements

This work was supported by the National Natural Science Foundation of China (No. 21276141), the State Key Laboratory of Chemical Engineering, China (No. SKL-ChE-12A05). The authors thank Dr. Wei Qi at the School of Chemistry and Chemical Engineering, Qufu Normal University, China, for the helpful discussion. The authors are also much obliged to the reviewers for the constructive suggestions on the great improvement of the work.

References

1 Z. L. Xie, R. J. White, J. Weber, A. Taubert and M. M. Titirici, *J. Mater. Chem.*, 2011, **21**, 7434-7442.

2 Y. Li, Z. Y. Fu and B. L. Su, *Adv. Funct. Mater.*, 2012, **22**, 4634-4667.

3 M. Q. Zhao, Q. Zhang, J. Q. Huang and F. Wei, *Adv. Funct. Mater.*, 2012, **22**, 675-694.

4 N. D. Petkovich and A. Stein, *Chem. Soc .Rev.*, 2013, **42**, 3721-3739.

5 W. Q. Wu, Y. F. Xu, H. S. Rao, H. L. Feng, C. Y. Su and D. B. Kuang, *Angew. Chem. Int. Ed.,* 2014, **53**, 4816-4821.

6 Y. Li, Z. Y. Fan, J. G. Lu and R. P. H. Chang, *Chem. Mater.*, 2004, **16**, 2512-2514.

7 X. Tao and X. Li, *Nano Lett.*, 2008, **8**, 505-510.

8 W. Zhu, X. Zhang, L. Xiang and S. Zhu, *Nanoscale Res Lett*, 2009, **4**, 724-731.

9 E. M. Elssfah, A. Elsanousi, J. Zhang, H. Song and C. Tang, *Mater. Lett.*, 2007, **61**, 4358-4361.

10 B. S. Xu, T. B. Li, Y. Zhang, Z. X. Zhang, X. G. Liu and J. F. Zhao, *Cryst. Growth Des.*, 2008, **8**, 1218-1222.

11 W. Zhu, Q. Zhang, L. Xiang and S. Zhu, *CrystEngComm*, 2011, **13**, 1654-1663.

12 W. Zhu, Q. Zhang, L. Xiang and S. Zhu, *Cryst. Growth Des.*, 2011, **11**, 709-718.

13 W. Zhu, R. Wang, S. Zhu, L. Zhang, X. Cui, H. Zhang, X. Piao and Q. Zhang, *ACS Sustainable Chem. Eng.*, 2014, **2**, 836-845.

14 R. Z. Ma, Y. Bando and T. Sato, *Appl. Phys. Lett.*, 2002, **81**, 3467-3469.

15 R. Z. Ma, Y. Bando, D. Golberg, T. Sato, *Angew. Chem. Int. Ed.*, 2003, **42**, 1836-1838.

16 Y. Zeng, H. B. Yang, W. Y. Fu, L. Qiao, L. X. Chang, J. J. Chen, H. Y. Zhu, M. H. Li and G. T. Zou, *Mater. Res. Bull.*, 2008, **43**, 2249-2247.

17 S. H. Chen, P. P. Jin, G. Schumacher, N. Wanderka, *Composites Sci. Technol.*, 2010, **70**, 123-129.

18 T. Kitamura, K. Sakane and H. Wada, J. *Mater. Sci. Lett.,* 1988, **7**, 467-469.

19 K. Sakane, H. Wada, T. Kitamura and M. Suzue, *Gypsum Lime,* 1991, **235**, 16-21.

20 K. Sakane, T. Kitamura, H. Wada and M. Suzue, *Adv. Powder Technol..* 1992, **3**, 39-46.

21 W. Zhu, L. Xiang, X. Zhang and S. Zhu, *Mater. Res. Innov.,* 2007, **11**, 188-192.

22 B. S. Xu, T. B. Li, Y. Zhang, Z. X. Zhang, X. G. Liu, and J. F. Zhao, *Cryst. Growth Des.,* 2008, **8**, 1218-1222.

23 L. Kumari, W. Li, S. Kulkarni, K. Wu, W. Chen, C. Wang, H. Vannoy, R. Leblanc, *Nanoscale Res. Lett.,* 2009, **5**, 149-157.

24 W. Zhu, Q. Zhang, L. Xiang, F. Wei, X. Sun, X. Piao and S. Zhu, *Cryst. Growth Des.,* 2008, **8**, 2938-2945.

25 W. Zhu, L. Xiang, Q. Zhang, X. Zhang, L. Hu and S. Zhu, *J.Cryst. Growth,* 2008, **310**, 4262-4267.

26 M. Titirici, R. White, C. Falco and M. Sevilla, *Energy Environ. Sci.*, 2012, **5**, 6796-6822.

27 H. Colfen and M. Antonietti, *Angew. Chem. Int. Ed.*, 2005, **44**, 5576-5591.

28 Z. Ma, J. Yu and S. Dai, *Adv. Mater.*, 2010, **22**, 261-285.

29 C. Reichardt, *Org. Process. Res. Dev.*, 2007, **11**, 105-113.

30 S. A. Forsyth, J. M. Pringle and D. R. MacFarlane, *Aust. J. Chem.*, 2004, **57**, 113-119.

31 X. Zhang, X. Zhang, H. Dong, Z. Zhao, S. Zhang and Y. Huang, *Energy Environ. Sci.*, 2012, **5**, 6668-6681.

32 G. Gao, Q. Zhang, K. Wang, H. Song, P. Qiu and D. Cui, *Nano Energy*, 2013, **2**, 1010-1018.

33 F. Teng, M. Chen, G. Li, Y. Teng, T. Xu, S. Mho and X. Hua, *J.Power Sources,* 2012, **202**, 384-388.

34 A. Chen, P. Gu, Z. Ni, *Mater. Lett.,* 2012, **68**, 187-189.

35 A. Chen, P. Gu, J. Hu. *Adv. Mater. Res.,* 2012, **486**, 260-264.

36 W. Zhu, L. Xiang, T. He and S. Zhu, *Chem. Lett.,* 2006, 35, 1158-1159.

37 J. Huang, G. Baker, H. Luo, K. Hong, Q. Li, N. Bjerrum and S. Dai, *Green Chem.*, 2006, **8**, 599-602.

38 X. D. Xie, and L. B. Liu, *Science Press, Beijing*, 1965, p. 54.

39 R. Chen, J. Yu and W. Xiao. *J. Mater. Chem. A*, 2013, **1**, 11682-11690.

40 W. Zhu, S. Zhu and L. Xiang, *CrystEngComm,* 2009, **11**, 1910-1919.

41 W. Zhu, X. Wang, X. Zhang, H. Zhang, Q. Zhang, *Cryst. Growth Des.,* 2011, **11**, 2935-2941.

42 A. Imanishi, S. Gonsui, T. Tsuda, S. Kuwabata and K. Fukui, *Phys. Chem. Chem. Phys.*, 2011, **13**, 14823-14830.

43 T. L. Greaves and C. J. Drummond, *Chem. Soc. Rev.*, 2013, **42**, 1096-1120.

44 L. Wang, L. X. Chang, L. Q. Wei, S. Z. Xu, M. H. Zeng and S. L. Pan, *J. Mater. Chem.*, 2011, **21**, 15732-15740.

45 Z. Zhu, X. Li, Y. Zeng, W. Sun, W. Zhu and X. Huang, *J. Phys. Chem. C*, 2011, **115**, 12547-12553.

46 J. Jiang, S. Yu, W. Yao, H. Ge and G. Zhang, *Chem. Mater.*, 2005, **17**, 6094-6100.

47 J. Zhou, S. Yang and J. Yu, *Colloids Surf. A*, 2011, **379**, 102-108.

48 I. D. Mall, V. C. Srivastava, N. K. Agarwal and I. M. Mishra, *Colloids Surf. A*, 2005, **264**, 17-28.

49 J. B. Fei, Y. Cui, J. Zhao, L. Gao, Y. Ynag and J. B. Li, *J. Mater. Chem.,* 2011, **21**, 11742-11746.

50 J. S. Wu, Y. H. Du, J. S. Wang, K. L. Huang, H. Y. Li, B. X. Liu. *J. Mater. Chem. A,* 2013, **1**, 9837-9847.

51 Z. Wei, R. Xing, X. Zhang, S. Liu, H. Yu and P. Li, *ACS Appl. Mater. Interfaces*, 2013, **5**, 598-604.

52 W. Cai, J. Yu and M. Jaroniec, *J. Mater. Chem.*, 2010, **20**, 4587-4593.

53 J. C. Hu, Z. Song, L. F. Chen, H. J. Ynag, J. L. Li and R. Richards, *J. Chem. Eng. Data,* 2010, **55**, 3742-3748.

54 A. Tadjarodi, M. Imani, H, Kerdari, *J. Nanostructure Chem.*, 2013, **3***,* 1-8.

55 V. S. Mane and P. V. Vijay Babu, *J. Taiwan Inst. Chem. Eng.*, 2013, **44**, 81-88.

56 X. C. Ynag, Z. Wang, M.X. Jing, R.J. Liu, L.N. Jin, X.Q. Shen. *Water Air Soil Pollut.* 2014, **225**, 1818.

57 L. Lian, L. Guo and C. Guo, *J. Hazard. Mater.*, 2009, **161**, 126-131.

58 H.-J. Cui, J.-W. Shi, B. Yuan and M.-L. Fu, *J. Mater. Chem. A*, 2013, **1**, 5902-5907.

59 T. K. Naiya, P. Chowdhury, A. K. Bhattacharya, S. K. Das, *Chem. Eng. J.,* 2009, **148**, 68-79.

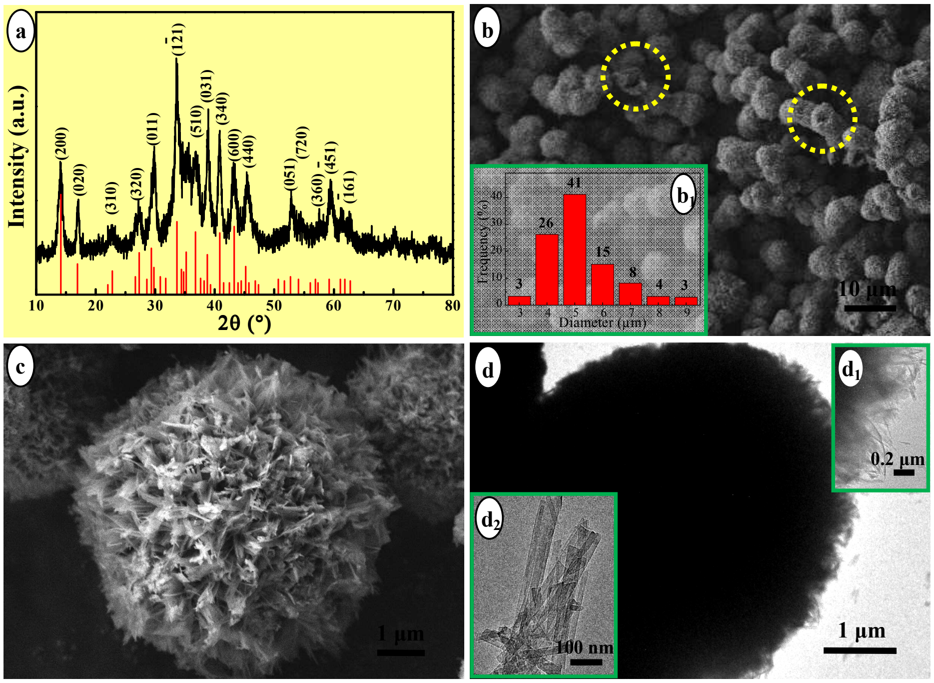

Fig. 1. XRD pattern (a), SEM (b, c) and TEM (d, d_1, d_2) images of the hierarchical porous $MgBO_2(OH)$ microspheres ionothermally synthesized at 150 ºC for 12.0 h. The vertical lines (a) indicate the standard pattern of the monoclinic $MgBO_2(OH)$ (JCPDS No. 39-1370). The inset (b_1) is the size distribution of the $MgBO_2(OH)$ microspheres.

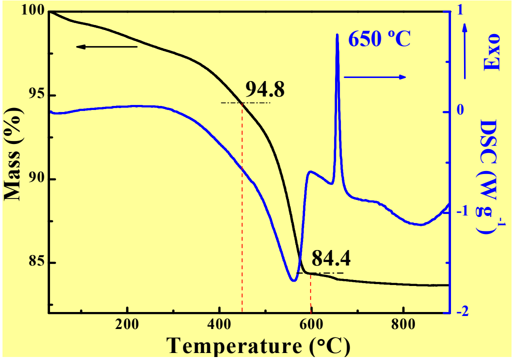

Fig. 2. TG-DSC curves of the hierarchical porous $MgBO_2(OH)$ superstructures ionothermally synthesized at 150 ºC for 12.0 h.

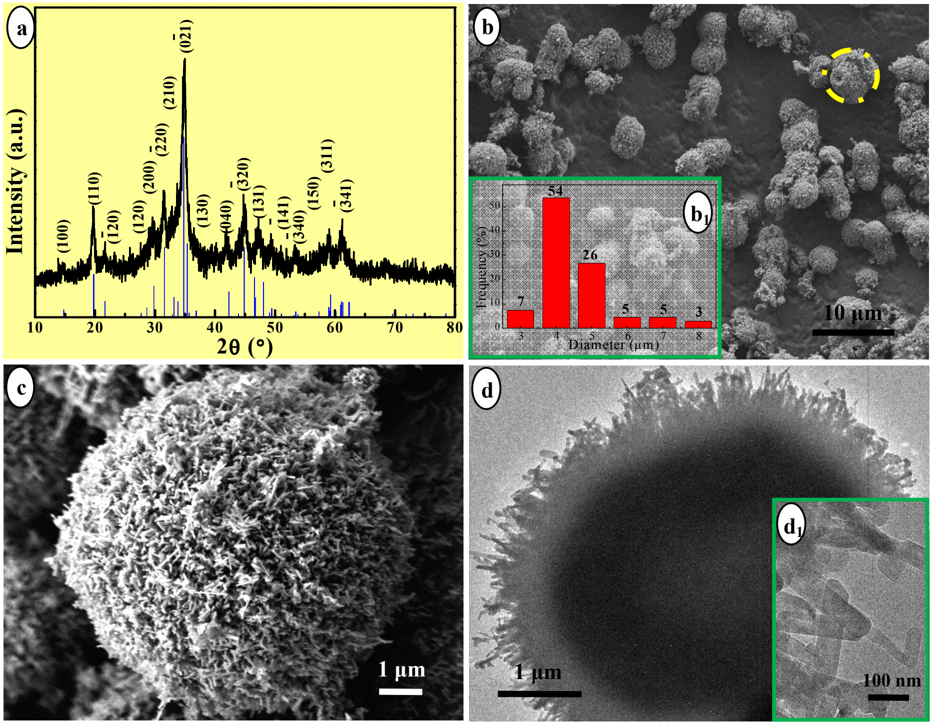

Fig. 3. XRD pattern (a), SEM (b, c) and TEM (d, d_1) images of the $Mg_2B_2O_5$ superstructures calcined at 600 ºC for 12.0 h (heating rate: 5 ºC min^{-1}). The vertical line in (a) is the standard pattern of the triclinic $Mg_2B_2O_5$ (JCPDS No. 73-2232). The inset is the size distribution of the $Mg_2B_2O_5$ superstructures.

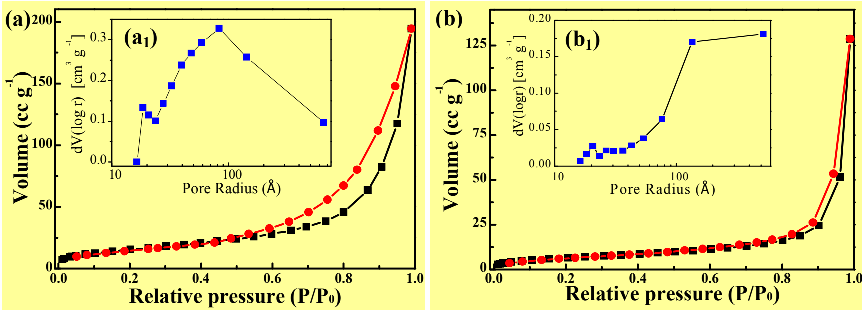

Fig. 4. Nitrogen adsorption-desorption isotherms (a, b) and the corresponding pore radius distribution curves (a_1, b_1) of the $MgBO_2(OH)$ (a, a_1) and $Mg_2B_2O_5$ (b, b_1) superstructures.

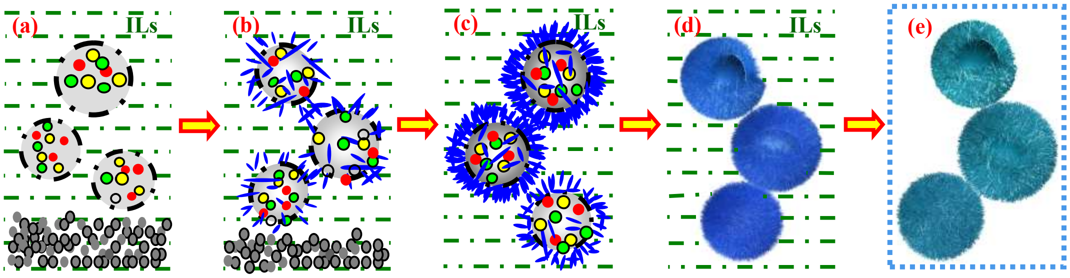

Fig. 5. The proposed formation mechanism of the hierarchical $MgBO_2(OH)$ and $Mg_2B_2O_5$ superstructures by the ionothermal-thermal conversion synthesis. (a) Water originated from the reactant led to spherical water bubbles or reservoirs within the ILs, which favored and trapped the continuously dissolved Mg^{2+}, $B(OH)_4^-$ and OH^- ions from the deposited solid reactants; (b) With the temperature increasing, Mg^{2+}, $B(OH)_4^-$ and OH^- ions reacted with each other, producing original rudimental 1D nanorod-like $MgBO_2(OH)$ nanostructures at the cost of continuously dissolution of the reactants; (c) The newly dissolved ions migrated into the reservoirs continuously, serving as the requisite nutrients for the heterogeneous or homogeneous nucleation and also pushing the pre-formed nanorods to move outwards to the interfaces between the water and ILs; (d) Hydrophilic effect of the nanorods' surfaces rendered the stable ionothermal confined self-organization of the nanorods, bring about the uniform hierarchical porous $MgBO_2(OH)$ microspheres; (e) Mild thermal conversion gave rise to the final hierarchical porous $Mg_2B_2O_5$ microspheres (●-Mg^{2+}, ●-$B(OH)_4^-$, ●-OH^-, ╲-$MgBO_2(OH)$, ╲-$Mg_2B_2O_5$).

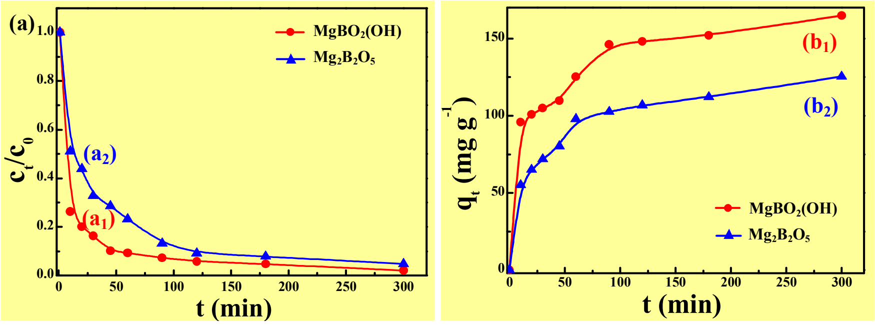

Fig. 6. Adsorption rate (a) and capacity (b) of the $MgBO_2(OH)$ (a_1, b_1) and $Mg_2B_2O_5$ (a_2, b_2) superstructures for CR removal as a function of the contact time, with an initial concentration of 50 mg L^{-1}.

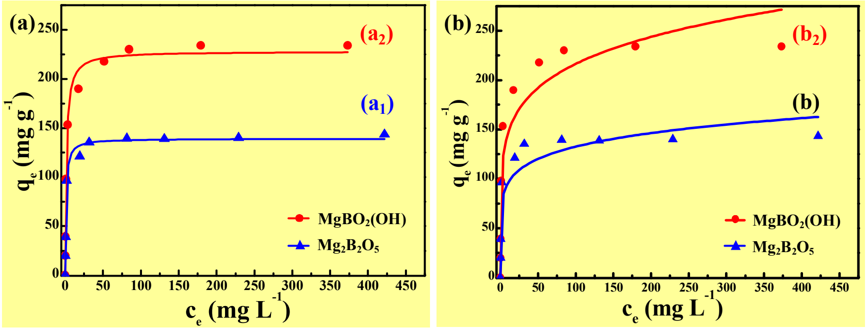

Fig. 7. The adsorption isotherms of CR onto the hierarchical porous MgBO$_2$(OH) (a$_2$, b$_2$) and Mg$_2$B$_2$O$_5$ (a$_1$, b$_1$) superstructures, fitted with Langmuir model (a$_1$, a$_2$) and Freundlich (b$_1$, b$_2$) model, respectively.

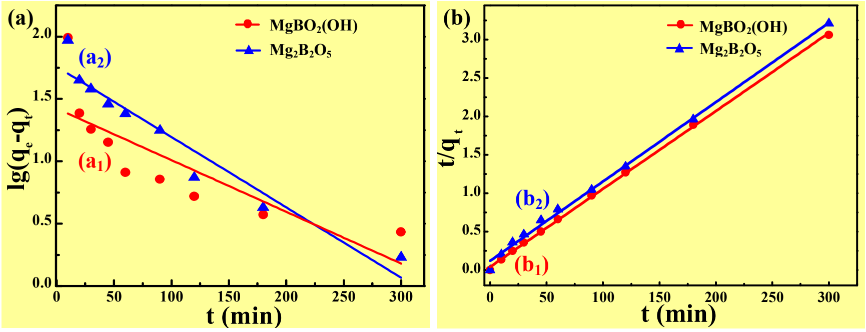

Fig. 8. Pseudo-first-order (a) and pseudo-second-order (b) kinetic plots of CR (50 mg L^{-1}) adsorption onto the hierarchical porous MgBO$_2$(OH) (a$_1$, b$_1$) and Mg$_2$B$_2$O$_5$ (a$_2$, b$_2$) superstructures.

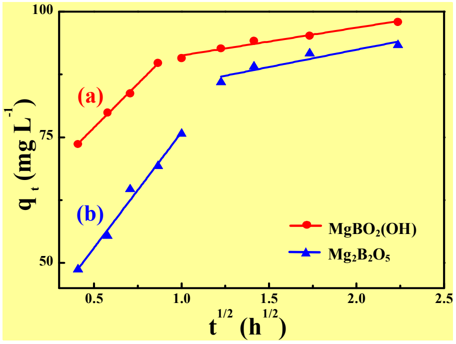

Fig. 9. Intra-particle diffusion model for adsorption of CR (50 mg L^{-1}) onto the hierarchical porous MgBO$_2$(OH) (a) and Mg$_2$B$_2$O$_5$ (b) superstructures.

Table 1. Comparison of the maximum adsorption capacities (q_m, mg g^{-1}) for CR on various adsorbents.

Adsorbents	S_{BET} (m^2 g^{-1})	q_m (mg g^{-1})	Reference
Eucalyptus wood saw dust	0.3742	31.25	55
Fe_3O_4 microspheres	71.5	42.55	48
Hierarchical urchin-like α-Fe_2O_3 nanostructures	69	66	49
γ-Al_2O_3/$Ni_{0.5}Zn_{0.5}Fe_2O_4$ microfibers	118.3	75.5	56
α-Fe_2O_3 hollow structures	32.9	93.55	50
Ca-bentonite	-	107.41	57
Hierarchical porous $Mg_2B_2O_5$ superstructures	24.20	139.3	this work
Hollow nestlike α-Fe_2O_3 spheres	152.42	160	51
Hierarchical spindle-like γ-Al_2O_3	149	176.7	52
Porous Mn/Fe_3O_4 nanowires	45.4	180	58
Hierarchical porous $MgBO_2(OH)$ superstructures	57.22	228.3	this work
MgO (111) nanoplates	198	303	53
CdO cauliflower-like nanostructure	104	588.2	54